

A kinematic study of the irregular dwarf galaxy NGC 4861 using H I and H α observations

J. van Eymeren^{1,2,3}, M. Marcelin⁴, B. S. Koribalski³, R.-J. Dettmar², D. J. Bomans², J.-L. Gach⁴, and P. Balard⁴

¹ Jodrell Bank Centre for Astrophysics, School of Physics & Astronomy, The University of Manchester, Alan Turing Building, Oxford Road, Manchester, M13 9PL, UK

e-mail: Janine.VanEymeren@manchester.ac.uk

² Astronomisches Institut der Ruhr-Universität Bochum, Universitätsstraße 150, 44780 Bochum, Germany

³ Australia Telescope National Facility, CSIRO, PO Box 76, Epping, NSW 1710, Australia

⁴ Laboratoire d'Astrophysique de Marseille, OAMP, Université Aix-Marseille & CNRS, 38 rue Frédéric Joliot-Curie, 13013 Marseille, France

Received 2 February 2009 / Accepted 20 July 2009

ABSTRACT

Context. Outflows powered by the injection of kinetic energy from massive stars can strongly affect the chemical evolution of galaxies, in particular of dwarf galaxies, as their lower gravitational potentials enhance the chance of a galactic wind.

Aims. We therefore performed a detailed kinematic analysis of the neutral and ionised gas components in the nearby star-forming irregular dwarf galaxy NGC 4861. Similar to a recently published study of NGC 2366, we want to make predictions about the fate of the gas and to discuss some general issues about this galaxy.

Methods. Fabry-Perot interferometric data centred on the H α line were obtained with the 1.93 m telescope at the Observatoire de Haute-Provence. They were complemented by H I synthesis data from the VLA. We performed a Gaussian decomposition of both the H α and the H I emission lines in order to search for multiple components indicating outflowing gas. The expansion velocities of the detected outflows were compared to the escape velocity of NGC 4861, which was modelled with a pseudo-isothermal halo.

Results. Both in H α and H I the galaxy shows several outflows, three directly connected to the disc and probably forming the edges of a supergiant shell, and one at kpc-distance from the disc. We measured velocity offsets of 20 to 30 km s⁻¹, which are low in comparison to the escape velocity of the galaxy and therefore minimise the chance of a galactic wind.

Key words. galaxies: individual: NGC 4861 – galaxies: irregular – galaxies: ISM – galaxies: kinematics and dynamics – galaxies: structure

1. Introduction

The low metal content of dwarf galaxies and the metal enrichment of the intergalactic medium (IGM) both suggest that mass loss triggered by star formation activity has to play a major role in the evolution of galaxies, especially of dwarf galaxies. These galaxies provide a perfect environment to study feedback processes as they show strong starburst activity, but are simple systems, which makes the interaction between stars and the interstellar medium (ISM) very efficient. Their gravitational potential is low, which supports the long-term survival of shells, filaments, and holes. This results in numerous ionised gas structures, sometimes up to kpc distances away from any place of current star formation (Hunter et al. 1993), visible on deep H α images. High-resolution long-slit echelle spectra revealed that most of them expand from the disc into the halo of their host galaxy (e.g., Martin 1998; van Eymeren et al. 2007), probably driven by stellar winds of, e.g., Wolf-Rayet stars and by supernovae explosions.

The final fate of the expanding gas is still a matter of discussion. The expansion into a very dense medium or a decrease of energy input could lead to a decrease of the expansion velocity so that the gas will eventually fall back onto the galactic disc (outflow). On the other hand, it is also possible that the energy input is high enough to accelerate the gas beyond the escape velocity of the host galaxy, which means that the gas might leave the gravitational potential by becoming a freely flowing wind (galactic wind).

So far, no clear evidence for a galactic wind in local dwarf galaxies has been found (Bomans 2005). This is supported by 2D calculations of multi-supernova remnants evolving in dwarf galaxies (Silich & Tenorio-Tagle 1998), which show that galaxies with an ISM mass of the order of $10^9 M_{\odot}$ keep their processed material, even their metals. However, hydrodynamic simulations by Mac Low & Ferrara (1999) reveal that at least the metals always have a high chance of being blown away, independent of the galaxy's mass. For low mass dwarf galaxies ($<10^9 M_{\odot}$), the chance rises that also some parts of the gas escape from the gravitational potential.

This is the second paper where we present the results of a detailed kinematic study of the neutral and ionised gas components in a sample of nearby dwarf galaxies. It is focused on the irregular dwarf galaxy NGC 4861. For our optical observations, we used a scanning Fabry-Perot interferometer centred on the H α line that provides us with a complete spatial coverage of the galaxy and relevant spectral information. For the H I analysis, we combined the VLA D array data by Wilcots et al. (1996) with VLA C array data. We added another VLA C array data set published by Thuan et al. (2004) to improve the *uv*-coverage and the sensitivity.

NGC 4861 is classified as an SB(s)m galaxy, although it shows no evidence for spiral structure (Wilcots et al. 1996). Its appearance in H α is dominated by the Giant Extragalactic H II region (GEHR) IZw 49 in the south-west at 12^h59^m00.4^s, +34°50'42", where most of the star formation occurs. A chain of small H II regions extends to the north-east forming a tail and

therefore giving the galaxy a cometary-shaped appearance. We adopt a distance of 7.5 Mpc (de Vaucouleurs et al. 1991).

High-resolution long-slit echelle spectra centred on the H α line of this galaxy were recently analysed by us (van Eymeren et al. 2007). We found a kpc-sized expanding supergiant shell (SGS4) around the GEHR, the blue-shifted component expanding with 110 km s⁻¹ and the red-shifted component with 60 km s⁻¹. The galaxy has also been studied in HI by Wilcots et al. (1996) as well as by Thuan et al. (2004). They report the detection of a small HI cloud, NGC 4861 B, at a deprojected distance of 4 kpc east from NGC 4861 that appears to have no optical counterpart.

This paper is organised as follows: the observations and the data reduction are presented in Sect. 2. Section 3 describes and compares the morphology of both gas components; Sect. 4 presents a kinematic analysis. In Sect. 5, different aspects are discussed, and Sect. 6 summarises the main results.

2. Observations and data reduction

2.1. The Fabry-Perot H α data

Fabry-Perot (FP) interferometry of NGC 4861 was performed on the 28th of February 2006 with the 1.93 m telescope at the Observatoire de Haute-Provence (OHP), France. We used the Marseille's scanning FP and the new photon counting camera (Gach et al. 2002). The field of view is 5'8" \times 5'8" on the 512 \times 512 pixels of the detector and is slightly limited by the interference filter to 5'5" \times 5'5", which results in a spatial resolution of 0'68 per pixel. The H α line was observed through an interference filter centred at the galaxy's rest wavelength of 6581 Å with a Full Width at Half Maximum (*FWHM*) of 10 Å. The free spectral range of the interferometer – 376 km s⁻¹ – was scanned through 24 channels with a sampling step of 15 km s⁻¹. The final spectral resolution as measured from the night sky lines is about 50 km s⁻¹. The seeing was about 3" to 4".

43 cycles were observed with an integration time of 10 s per channel, hence 240 s per cycle and 172 min in total. We used a neon lamp for the phase and the wavelength calibration. The data reduction was done with the software package ADHOCw¹, written by Jacques Boulesteix: first, all cycles were checked for bad data. Afterwards, the remaining cycles were added channel per channel. A phase map was created from the exposure of a neon calibration lamp in order to define an “origin” channel, i.e., a channel where all pixels have their intensity peaking at maximum. As this channel varies across the field of view, intensity maxima of many pixels had to be shifted to other channels in order to get the same wavelength origin for all pixels. As a next step, the phase map was used in order to perform the wavelength calibration. In order to match the average seeing at OHP, we applied a Gaussian spatial smoothing with a *FWHM* of 3 pixels in *x* and *y*. Additionally, we spectrally smoothed the data with a Gaussian *FWHM* of 3 channels. As a last step, we measured the night sky at different positions across the field of view and subtracted an average value from every pixel. As the sky intensity varies over the field of view due to the shape of the interference filter, this approach led to residuals of the OH lines in the spectra. However, we carefully checked their positions for the chosen free spectral range and the neighbouring ones and conclude that the H α emission of NGC 4861 is not contaminated by the night sky. We also checked the instrumental response by looking at the profile of the neon calibration line. We found that the calibration

line is symmetric. Assuming that the FP response is similar for H α and the wavelength range where the calibration line has been observed, we expect no artificial wings in the observed H α emission lines.

The H α intensity distribution and the velocity field were created from the H α cube by removing all emission below a 2.5 σ threshold.

2.2. Optical imaging

We use a fully reduced 900 s *R*-band image, observed with the WIYN 3.5 m telescope at Kitt Peak, which was kindly provided by E. Wilcots. Additionally, we work with a fully reduced 1200 s H α image which is part of the “Palomar/Las Campanas Imaging Atlas of Blue Compact Dwarf Galaxies” by Gil de Paz et al. (2003).

In order to search for an optical counterpart of the HI cloud NGC 4861 B, we obtained a 90 min *V*-band image with the 2.2 m telescope at Calar Alto equipped with CAFOS on the 3rd of March 2008. The data reduction was performed by us using the software package IRAF and included standard procedures of overscan- and bias-subtraction as well as a flatfield correction. Additionally, we removed cosmic rays by running the IRAF version of L.A. Cosmic² (van Dokkum 2001).

2.3. The HI data

VLA C and D array data were kindly provided by E. Wilcots. They are flux and bandpass calibrated using periodic observations of 3C 147. Further details concerning the data reduction can be found in Wilcots et al. (1996). We complemented the data by an archival VLA C array data set in order to improve the sensitivity and the uv-coverage. Flux and bandpass calibrations using the calibrator source 3C 286 were done by us in AIPS. The bandpass represents the instrumental response. By subtracting it from the *uv* data, we made sure that the HI emission line profiles are not affected by artificial structures. The continuum was subtracted from the HI emission by using a first order fit to the line-free channels.

The three data sets were then combined by taking into account the different pointings. The *invert* task in MIRIAD is very well suited for mosaicing data so that we combined, inverted, cleaned, and restored the cube in MIRIAD. The final data cube has a synthesised beam size of 31" \times 30" after using a “natural” weighting. The spectral resolution is 5.2 km s⁻¹. We applied a 3-point Hanning smoothing, which improved the noise level from 0.6 to 0.5 mJy beam⁻¹.

The moment maps were created from the un-smoothed cube and again, emission below a 2.5 σ threshold was removed. The processing and the subsequent analysis of the HI data was performed with GIPSY³ (van der Hulst et al. 1992).

3. General morphology

3.1. Stellar and ionised gas distribution

The *R*-band image and the H α image from the Palomar/Las Campanas survey are shown in Fig. 1. The H α luminosity is dominated by the GEHR in the south. A chain of smaller H II regions extends to the north-east ending in a ring-like structure at the northernmost tip, which is located at the outer edge of

¹ <http://www.oamp.fr/adhoc/>

² <http://www.astro.yale.edu/dokkum/lacosmic/>

³ The Groningen Image Processing System.

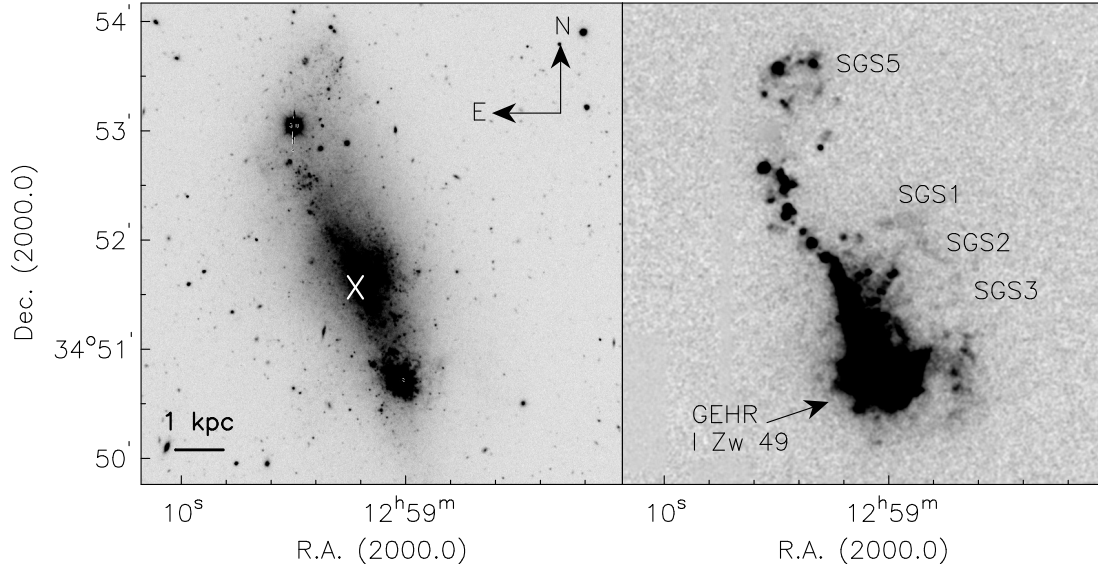


Fig. 1. *Left panel:* R-band image of NGC 4861 as obtained from the WIYN 3.5 m telescope. The optical centre is indicated by a white cross. *Right panel:* continuum-subtracted H α image from the Palomar/Las Campanas survey. The contrast is chosen in a way to emphasise the large-scale structures. The supergiant shells are numbered according to van Eymeren et al. (2007) and Sect. 3.1. In order to stress weaker structures and to differentiate them from the noise, we used adaptive filters based on the H-transform algorithm (Richter et al. 1991).

the stellar distribution. No star cluster seems to be associated with it. With a diameter of about 1 kpc, it belongs to the large-scale structures in this galaxy (note that the galaxy has an optical size of about 9 kpc \times 3 kpc at the adopted distance of 7.5 Mpc). Following the classification and numbering of van Eymeren et al. (2007), it is catalogued as supergiant shell SGS5.

Figure A.1 shows an enlargement of the continuum-subtracted H α image that emphasises the small-scale structure close to the disc. Most of the filaments can be found on the western side of the galaxy. Overlaid in grey are the FP H α intensity contours at 0.5 (3σ), 5, 10, 20, 50, 100, and 300 (arbitrary units). Although the FP image is quite noisy, all important filaments and shells can be detected.

3.2. The distribution of the neutral gas

Figure 2 shows the HI channel maps, superposed on a greyscale presentation of the R-band image. The white cross in the first channel marks the optical centre of the galaxy (see Table 1). The beam is placed in the lower left corner of the same channel. The corresponding heliocentric velocities are indicated in the upper right corner of each channel map. At first glance, it can be seen that the HI emission is much more extended than the optical content of the galaxy. The distribution is quite smooth with an asymmetry to the east.

The integrated HI intensity distribution is displayed on the upper left panel of Fig. 3. As already seen on the channel maps, it is symmetrically distributed, except for the eastern part, with several maxima along the north-south axis. The distortion in the east is most probably linked to the HI cloud NGC 4861 B. Its morphology will be discussed separately in Sect. 3.4.

3.3. A comparison of the neutral and ionised gas distribution

We now compare the morphology of the ionised and neutral gas by plotting the HI intensity contours over the continuum-subtracted H α image (see Fig. 4). The overlay shows that the optical galaxy lies in the centre of the HI distribution. The HI intensity maxima all coincide with the optical extent. However,

Table 1. HI properties as measured from the VLA data.

Parameters [Unit]	NGC 4861	NGC 4861 B
optical centre ^a :		
α (J2000.0)	12 ^h 59 ^m 02.3 ^s	
δ (J2000.0)	+34°51'34"	
D [Mpc] ^b	7.5	
dynamic centre ^c :		
α (J2000.0)	12 ^h 59 ^m 01.4 ^s	12 ^h 59 ^m 32.6 ^s
δ (J2000.0)	+34°51'43"	+34°51'15"
v_{sys} [km s ⁻¹] ^c	835 \pm 1	791
i [°] ^c	65 \pm 3	65
PA [°] ^c	16 \pm 3	244
v_{rot} [km s ⁻¹] ^c	46	4.4
F_{HI} [Jy km s ⁻¹]	36.08	0.30
M_{HI} [$10^8 M_{\odot}$]	4.79	0.04
HI diameter [']	7.0 \times 4.9	1.6 \times 0.9
" [kpc]	15.2 \times 10.7	3.6 \times 1.9
HI / opt. ratio	2.3 \times 5	...
$\langle\sigma\rangle$ [km s ⁻¹]	14	7
σ_{Peak} [km s ⁻¹]	22.8	9.9
$r_{\text{HI,max}}$ [kpc]	10.9	2.7
M_{dyn} [$10^9 M_{\odot}$]	5.4	0.012

^a Data from NED; ^b distance from de Vaucouleurs et al. (1991); ^c derived by fitting a tilted-ring model to the HI data. In case of NGC 4861, where all parameters were fitted iteratively, the error weighted mean values plus uncertainties are given. The errors of the dynamic centre position are far below one beam size. The parameters of NGC 4861 B were estimated from fitting ellipses to the HI distribution.

the HI column density coinciding with the GEHR is lower than the maxima along the tail. Furthermore, the HI peak intensity is by more than one beam size offset with respect to the centre of the GEHR. The lower HI column density indicates that a significant part of the neutral gas has already been ionised, which resulted in the huge luminous H II region. Such an offset has also been found in other galaxies (IC 10, NGC 2366) and has been explained by sequential star formation (Hodge et al. 1994).

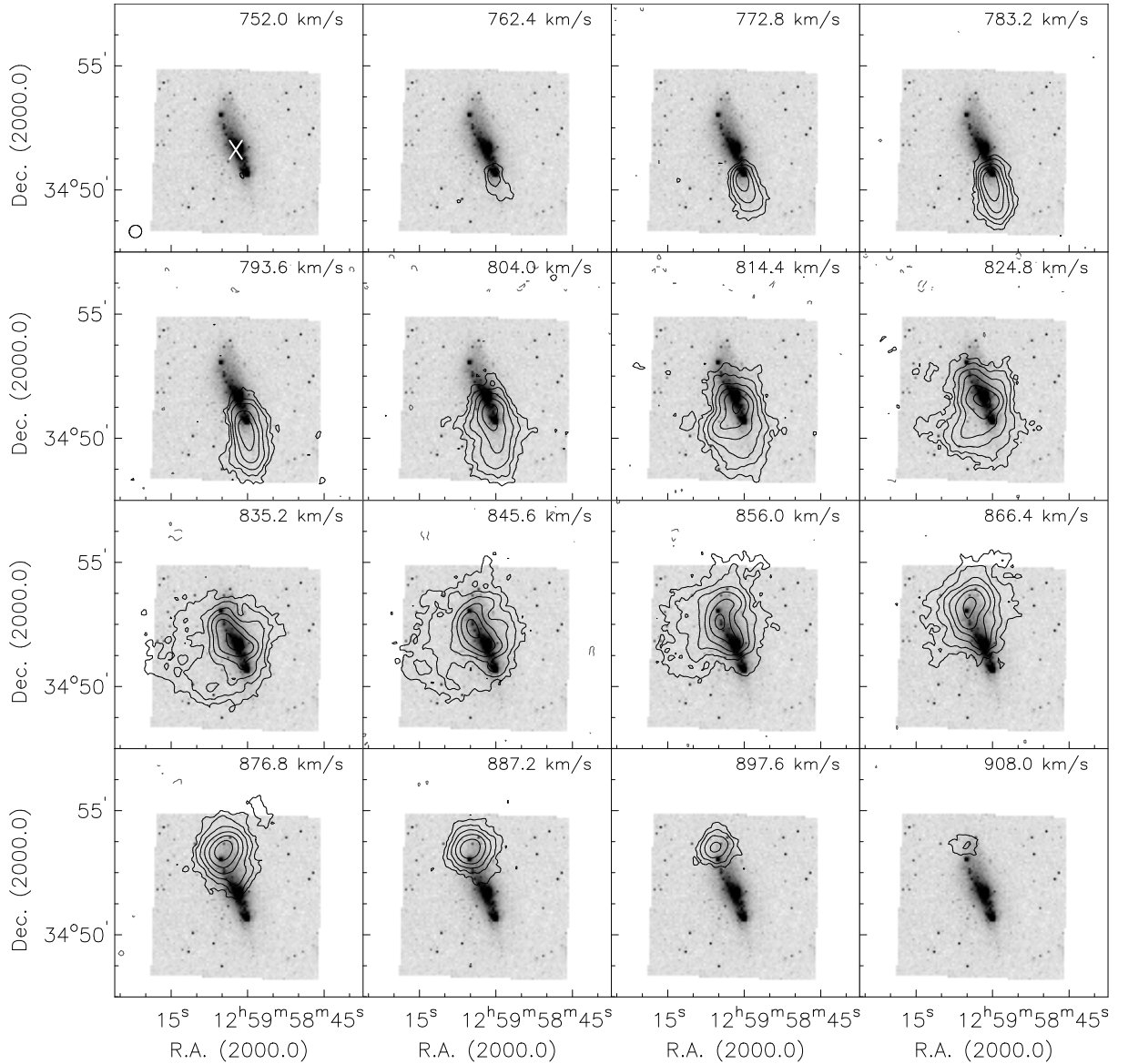


Fig. 2. HI channel maps of NGC 4861 (contours) as obtained from the VLA using a “natural” weighting, superposed on the *R*-band image. A 3-point Hanning smoothing was applied to the cube improving the noise level from 0.6 to 0.5 mJy beam⁻¹. The original channel spacing is 5.2 km s⁻¹. Contours are drawn at -1.5 (-3σ), 1.5 (3σ), 3, 6, 12, 24 and 48 mJy beam⁻¹. The synthesised beam is placed in the lower left corner of the first channel map. The optical centre of the galaxy is marked by a white cross in the same channel map. The corresponding heliocentric velocities are shown in the upper right corner of each channel.

The three main HI maxima coincide with several of the smaller H II regions along the tail. Close to the supergiant shells SGS1, SGS2 and SGS3 as well as east of the GEHR, the gradient of the intensity decrease is different from the overall gradient. In both cases, the gradient is flatter, which means that the gas density is higher than in the surroundings. This might indicate outflowing gas and indeed, the kinematic analysis below will show that these two regions harbour expanding gas structures.

3.4. Morphological features of the HI cloud NGC 4861 B

NGC 4861 has a small companion east of the main body at a deprojected distance of 4 kpc (Fig. 3). The HI mass was measured to be $4 \times 10^6 M_{\odot}$ (see Table 1). It seems to interact with the main HI complex as the large-scale HI distribution is extended in its direction and the velocity field is distorted. Figure 6 shows the HI channel maps, superposed on a greyscale presentation of our *V* band image. NGC 4861 B can be detected over a

velocity range of 26 km s⁻¹, although the column density is quite low. The gas is smoothly distributed.

Previous studies using DSS images could not detect an optical counterpart of this cloud (e.g., Wilcots et al. 1996). However, we have obtained a significantly deeper *V*-band image of this field (see Sect. 2.2), which is shown in Fig. 5. Overlaid are the outer HI intensity contour at 0.01 Jy beam⁻¹. No stellar association that could be connected to NGC 4861 B can be seen. Assuming that the size of a possible stellar disc equals the HI extent of 1.6×0.9 (see Table 1), we derived an upper limit for the integrated flux in the *V*-band image of $m_V < 24.3$ mag and $M_V < -6.54$ mag respectively, which makes the existence of a stellar component very unlikely.

4. Kinematic analysis

Spectra extracted from the H α and the HI data cubes show that both emission lines are sometimes split into several components.

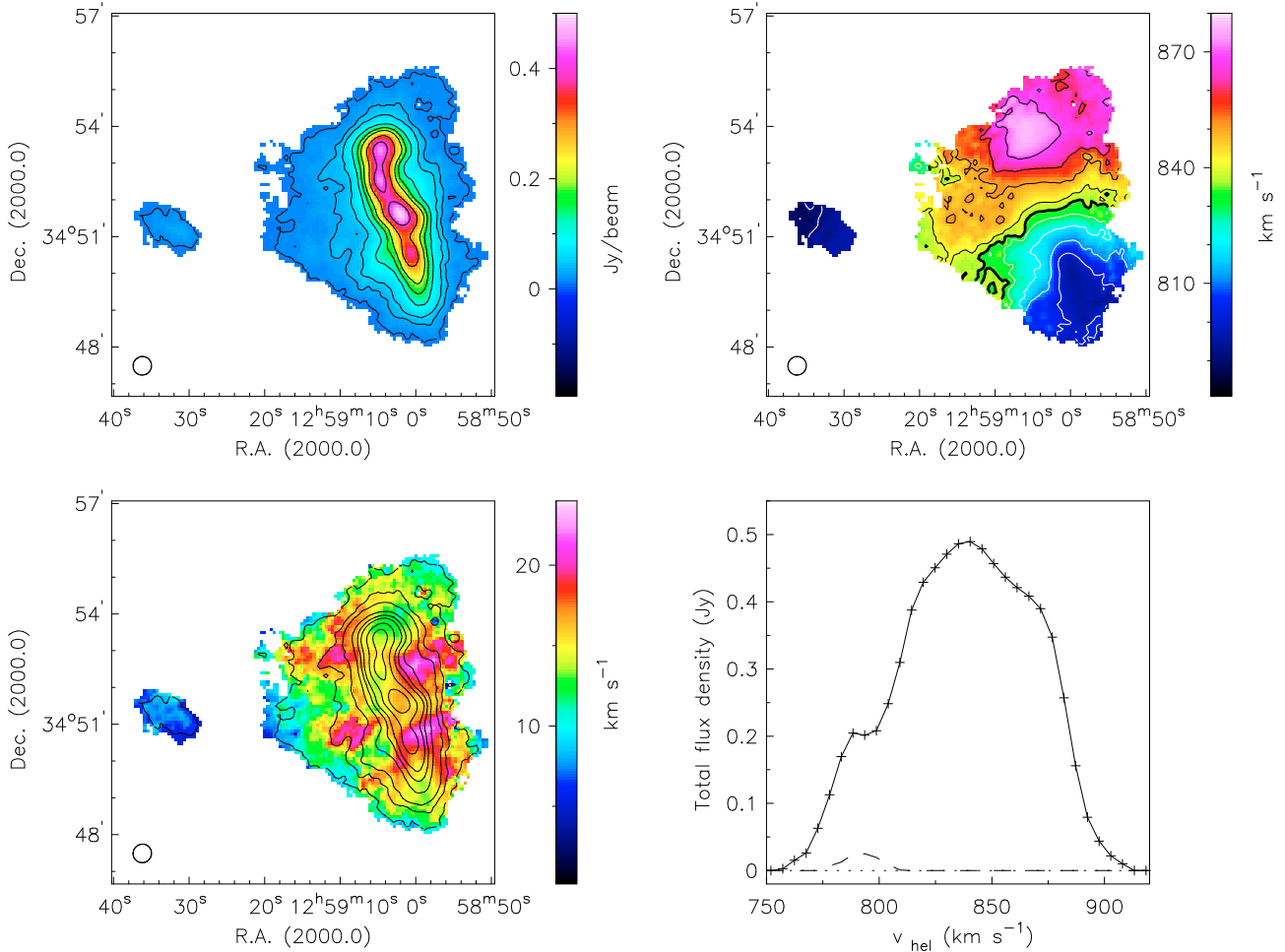


Fig. 3. The HI moment maps of NGC 4861 using “natural” weighting, which leads to a synthesised beam of $31'' \times 30''$. *Top left:* the HI intensity distribution. Contours are drawn at 0.01, 0.03, 0.05, 0.1, 0.15, 0.2, 0.3, 0.4 Jy beam $^{-1}$ where 10 mJy beam $^{-1}$ correspond to a column density of 1.6×10^{21} atoms cm $^{-2}$. *Top right:* the HI velocity field. Contours are drawn from 790 to 870 km s $^{-1}$ in steps of 10 km s $^{-1}$. The systemic velocity of 835 km s $^{-1}$ is marked in bold. *Bottom left:* the velocity dispersion, overlaid are the same HI intensity contours as mentioned above. *Bottom right:* the global intensity profile of the galaxy (solid line) and the HI cloud NGC 4861 B (long-dashed line). The short-dashed line marks zero intensity.

In order to take all gas components into account and to measure their properties, especially their velocities, we performed a Gaussian decomposition by interactively fitting the H α and HI emission with the IRAF task *splot*. Only detections above a 2.5σ limit were considered. All given velocities are heliocentric velocities measured along the line of sight.

4.1. The H α velocity field

Figure 7, upper panel shows the resulting H α velocity field with the component of highest intensity plotted. The overall velocity gradient runs from the south-west with velocities of about 800 km s $^{-1}$ to the north-east with velocities of about 870 km s $^{-1}$. This fits well with the systemic velocity measured from the HI data of about 835 km s $^{-1}$ (see below) and gives the ionised gas a rotation velocity of 35 km s $^{-1}$.

Several deviations from the overall rotation become immediately visible (indicated by black ellipses in the H α velocity field, corresponding example spectra are shown on the lower panel of Fig. 7): first, we detected a strong blue- and a weaker red-shifted component in the south of the GEHR (spectrum a, black solid line). The H α line is very broad and asymmetric and can be well fitted with two Gaussians, one at about 780 km s $^{-1}$ (blue (dark grey) long-dashed line), which is 30 km s $^{-1}$

blue-shifted with respect to the overall velocity gradient, and one at about 840 km s $^{-1}$ (red (light grey) long-dashed line), which is red-shifted by 30 km s $^{-1}$ with respect to the overall velocity gradient. The sum of both Gaussian fits is plotted with a green (light grey) short-dashed line and is in good agreement with the observed spectrum.

A strong red-shifted and a weaker blue-shifted component can be seen in the north of the GEHR (spectrum b). Again, both gas components are expanding with about 30 km s $^{-1}$ in comparison to their surroundings, which means that they probably belong to the blue- and red-shifted gas detected in the south of the GEHR.

Along the chain of HII regions to the north-east of the galaxy, slightly red-shifted gas seems to flow out of the disc in the direction of the supergiant shells located in the west (see Fig. 1, right panel). These three supergiant shells are kinematically separated: SGS1 and SGS2 are red-shifted with an expansion velocity of 30 km s $^{-1}$ (spectrum c), whereas SGS3 follows the rotation velocity.

The velocities in the area of SGS5 also follow the rotation of the galaxy. We found an indication of a blue-shifted component with a velocity offset of about 80 km s $^{-1}$ with respect to the main component (spectrum d).

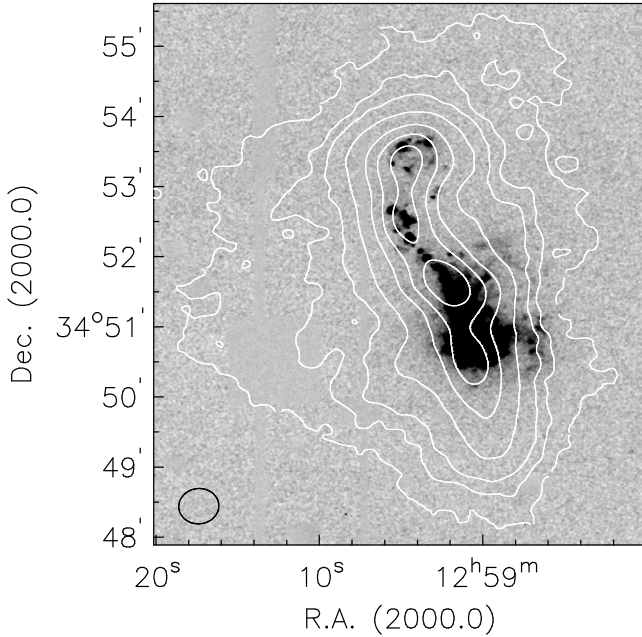


Fig. 4. A comparison of the H α and the HI morphology. The continuum-subtracted H α image is displayed. Overlaid in white are the HI intensity contours at 0.01, 0.03, 0.05, 0.1, 0.2, 0.3, and 0.4 Jy beam $^{-1}$.

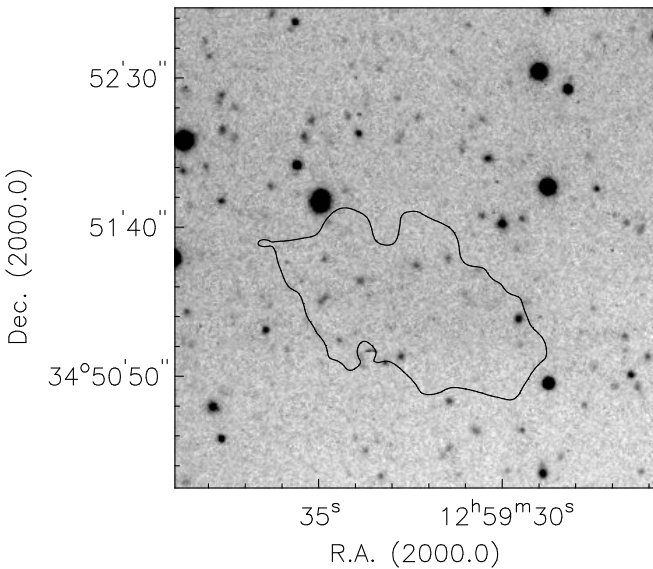


Fig. 5. Deep V-band image of the area of NGC 4861 B. Overlaid in black is the outer HI intensity contour of the HI cloud at 0.01 Jy beam $^{-1}$.

Note: except for the GEHR and the area of SGS5, we either detected only one expanding component, which then dominated the spectrum, or no outflows at all. Therefore, we only show the velocity field of the components of highest intensity. Furthermore, the instrumental response of the FP could cause artificially broader H α lines (e.g., Moiseev & Egorov 2008). To account for this effect, the fitted Gaussians have to be convolved with the instrumental profile. We compared pure Gaussian fits with convolved fits and found that the values of the emission line peaks remain unchanged, which is in agreement with the results by Moiseev & Egorov (2008). However, the H α velocity

dispersion might change significantly so that we do not mention any values in this paper.

4.2. The HI velocity field

The upper right panel of Fig. 3 shows the HI velocity field which looks fairly regular with a gradient rising from the south-west with velocities of about 795 km s $^{-1}$ to the north-east with velocities of about 870 km s $^{-1}$. As already mentioned by Wilcots et al. (1996), the isovelocity contours close at both ends of the galaxy, which is an indication for a declining rotation curve, possibly caused by a bar. We detected two major deviations from the rotation, the faint eastern part which does not show any regular velocity pattern, and the small HI cloud NGC 4861 B in the east which is offset by about 60 km s $^{-1}$ with respect to the velocity of the main body, suggesting that it is not rotating in the disc.

The HI velocity dispersion map (Fig. 3, lower left panel) shows altogether four maxima. The two areas of high dispersion to the east are probably caused by an interaction between the isolated HI cloud and the main body. The other two dispersion peaks might indicate an additional gas component. The overlay of the HI intensity contours reveals that the HI maxima are clearly offset from the regions of high dispersion except for the southernmost peak. All four dispersion maxima have velocities of 20 to 22 km s $^{-1}$, the median value lies at 14 km s $^{-1}$.

4.3. The HI rotation curve

In order to investigate the fate of the gas, we need to know some of the kinematic parameters of NGC 4861 like its inclination or its rotation velocity. Therefore, we derived a rotation curve from the HI data by fitting a tilted-ring model to the observed velocity field.

At the beginning, initial estimates for the kinematic parameters had to be defined, which were obtained by interactively fitting ellipses to the HI intensity distribution using the GIPSY task *ellfit*. These were then used as an input for the tilted-ring fitting routine *rotcur* (Begeman 1989). The width of the rings was chosen to be half the spatial resolution, i.e., 15'' in this case. In order to get the most precise values, three different approaches were made by always combining receding and approaching side. First, the initial estimates were all kept fixed. The resulting curve is indicated by the green (light grey) symbols in Fig. 8, upper left panel. In a second approach, the parameters were iteratively defined for all rings by keeping all parameters fixed except for the one we wanted to measure. Up to a radius of 200'', which corresponds to a distance of 7 kpc from the dynamic centre, no significant deviation or a sudden change of any of the parameters was noticed so that an average value (given in Table 1) was taken for each parameter (black symbols). In this approach, a rotation curve was also measured for receding and approaching side alone, indicated by the error bars of the black symbols. As a last approach, the so derived parameters were all left free in order to reproduce the result of the second approach (red (dark grey) symbols).

In the inner 200'', the green (light grey) symbols are in very good agreement with the black ones. From a radius of 200'' on, the differences become larger. The reason for this is that the filling factors of the rings drop from about 1 to about 0.5 at a radius of 200'', which leads to a higher uncertainty in calculating the rotation velocity. Therefore, every value above 200'' has to be treated with care. The red (dark grey) symbols only agree well within a radius of about 150''.

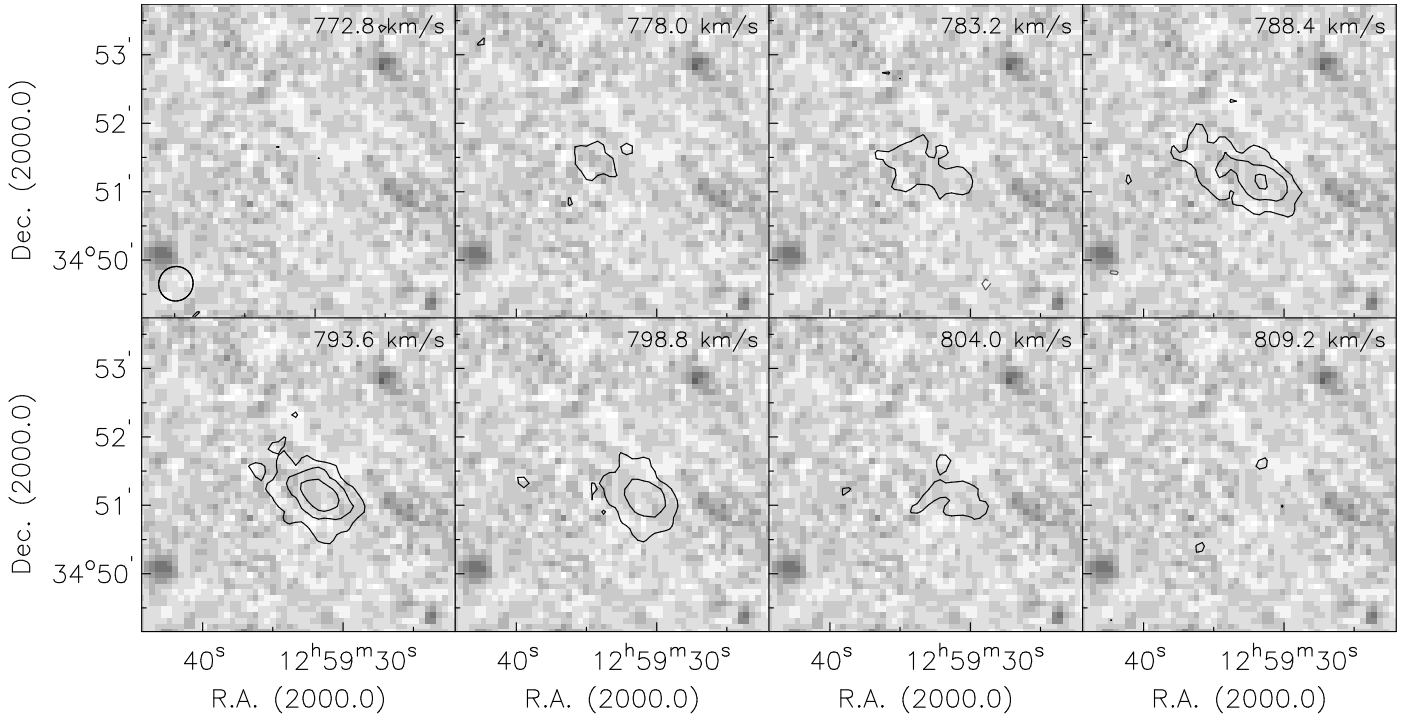


Fig. 6. HI channel maps of NGC 4861 B (contours), superposed on our V-band image. No smoothing was applied. Contours are drawn at -2 (-3σ), 2 (3σ), 4 , and 6 mJy beam $^{-1}$. Otherwise the same as Fig. 2.

In the inner $100''$, the velocity gradient is very steep and linear, indicating solid body rotation, which characterises dwarf galaxies. Above $100''$, the curve shows a plateau with a tendency to decline. The new rise at a radius of about $240''$ is certainly due to the sparsely filled tilted rings (as mentioned above). On the other hand, the disturbed gas in the eastern parts of the galaxy probably also causes a rise in velocity.

The best-fitting parameters from the iterative approach are given in Table 1. We derived an inclination of 65° , a position angle of 16° , and a systemic velocity of 835 km s $^{-1}$. These values are in good agreement with observations by Thuan et al. (2004) who measured v_{sys} to be 833 km s $^{-1}$ and a position angle of 17° . However, their inclination of 82° is significantly higher than our value. They also derived a higher value of v_{rot} (54 km s $^{-1}$ in comparison to 46 km s $^{-1}$ measured by us), which cannot be explained by the difference in inclination alone. Nevertheless, our result confirms the one of Thuan et al. (2004), which is that the rotation velocity measured by Wilcots et al. (1996) of 80 km s $^{-1}$ (i of 67°) is much too high.

In order to prove the reliability of the derived parameters, a model velocity field with the best-fitting values was created (Fig. 8, lower left panel) and subtracted from the original velocity field (upper right panel). The residual map can be seen on the lower right panel of Fig. 8. The overall velocity field is very well represented by our derived parameters except for the extension in the east of the galaxy. Here, the residuals reach absolute values of 15 to 20 km s $^{-1}$ in comparison to a general value of ± 5 km s $^{-1}$. As already mentioned before, this extension in combination with the disturbed velocity field is likely to be caused by an interaction with the small HI cloud NGC 4861 B to the east of the main body. Its kinematics are analysed in Sect. 4.5.

4.4. Comparison of the neutral and ionised gas kinematics

The H α velocity field (see Fig. 7, upper panel) shows three major deviations from the overall rotation velocity, one in the south

of the GEHR, one north of the GEHR, and one close to SGS1. In order to compare the velocities of the ionised gas with the velocities of the neutral gas, the HI velocity field was subtracted from the H α velocity map. Therefore, the FP data were smoothed to fit the spatial resolution of the HI data of $31'' \times 30''$. The resulting residual map is shown in Fig. 9. At most positions, the absolute value of the residuals is below 10 km s $^{-1}$, which means that the velocities of the neutral and ionised gas are generally in good agreement. The ionised gas in the southern part of the GEHR is blue-shifted with a velocity offset of about 25 km s $^{-1}$ relative to HI. The ionised gas of SGS1 and SGS2 is red-shifted with a velocity offset of about 30 km s $^{-1}$. Additionally, some red-shifted gas can be seen north of the GEHR, also with a velocity offset of about 30 km s $^{-1}$.

The areas of high HI velocity dispersion coincide fairly well with the regions of expanding ionised gas. Therefore, we decided to have a closer look at the kinematics of the neutral gas. We performed a Gaussian decomposition of the HI velocities by averaging the velocities over one beam size. The result is shown in Fig. 10: the components of highest intensity are presented in the middle panel. Overlaid in white are the HI velocity dispersion contours at 18 and 22 km s $^{-1}$ and the outer H α intensity contour in black. For a comparison, the blue- and red-shifted components are shown on the left and right panel respectively. Note that regions where we did not find a blue- or red-shifted component were filled with the main component. Four example spectra extracted from the HI cube at roughly the same positions as the H α spectra (see Fig. 7) are displayed in Fig. 11 together with the Gaussian fits for the single components (long-dashed blue (dark grey) and red (light grey) lines) and the resulting sum (short-dashed green (light grey) lines).

Looking at the southern edge of the optical galaxy, a blue-shifted component is detected with a heliocentric line of sight velocity of about 786 km s $^{-1}$. The main component at this position has a velocity of about 812 km s $^{-1}$. The H α velocity field shows at the same position a blue-shifted outflow with velocities

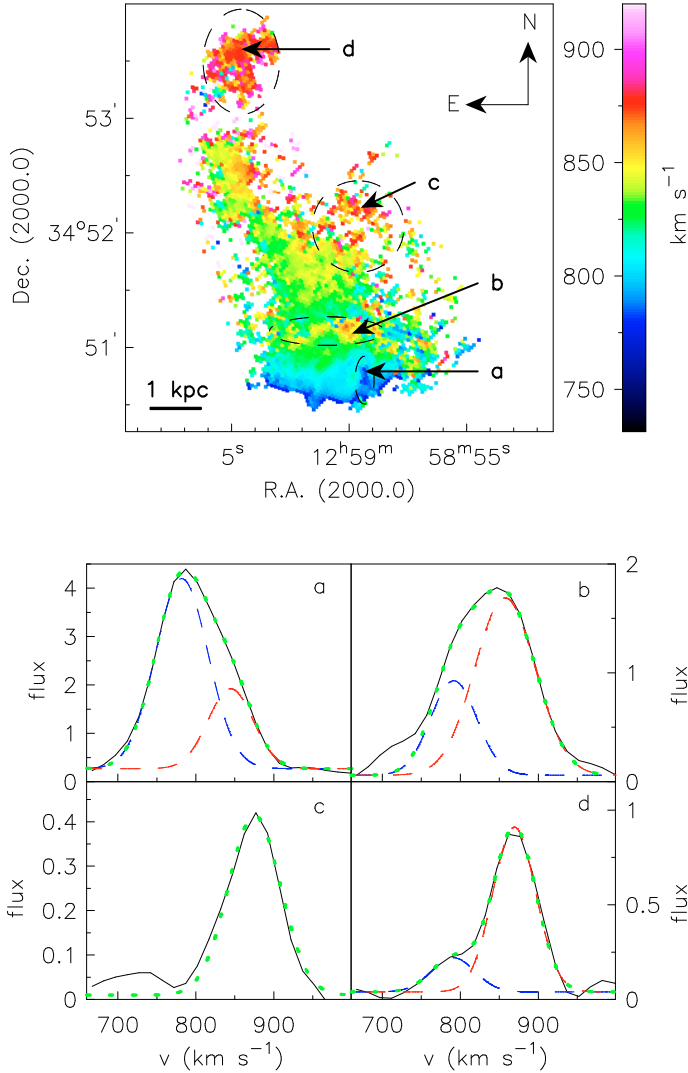


Fig. 7. The H α velocity field of NGC 4861. *Upper panel:* the velocity distribution of the strongest component. Significant deviations from the rotational gradient are illustrated by black ellipses. *Lower panel:* four example spectra (black solid lines) extracted from different areas across the galaxy, which show the flux in arbitrary units vs. the line of sight velocity. The H α line is often split into two components (blue (dark grey) long-dashed lines and red (light grey) long-dashed lines). The sum of both Gaussian fits is plotted with green (light grey) short-dashed lines. The following detections are displayed: **a)** the blue- and red-shifted outflows south of the GEHR; **b)** the blue- and red-shifted counterparts north of the GEHR; **c)** the red-shifted supergiant shells; **d)** the potential blue-shifted component at SGS5.

of about 780 to 790 km s⁻¹, which is in good agreement with the HI data. Additionally, we detected a red-shifted component at about 840 km s⁻¹ in the H α spectrum (see Fig. 7, spectrum a). At the same position, the Gaussian decomposition of the HI profiles also reveals gas at about 837 km s⁻¹, which is, however, not as extended as the blue-shifted gas. The blue-shifted outflow has already been detected in HI by Thuan et al. (2004) who suggested that this gas had been moved away from the GEHR, driven by stellar winds and SNe over the last 1600 yr.

As already mentioned in Sect. 4.1, the northern part of the GEHR shows a blue- and a red-shifted component in H α with a velocity offset of about 30 km s⁻¹. Figure 11, spectrum b only shows some red-shifted emission at the same position with velocities of about 837 km s⁻¹, which corresponds to an offset of about 25 km s⁻¹ with respect to the main HI component.

The region west of NGC 4861 where the three supergiant shells are located reveals a red-shifted component (see Fig. 10, right panel, Fig. 11, spectrum c). The velocities vary between 860 and 870 km s⁻¹ in comparison to the main component of 830 to 840 km s⁻¹, which is comparable to the ionised gas as the H α velocity map shows a red-shifted component of 860 to 870 km s⁻¹.

At the position of SGS5, a blue-shifted component with an expansion velocity of 20 km s⁻¹ was detected in addition to the main component, which is much lower than measured in H α .

4.5. HI kinematics of NGC 4861 B

In order to study the HI kinematics of NGC 4861 B, we performed the same analysis for the HI cloud as for the whole galaxy (see Sect. 4.3) treating the cloud as an individual system. As we were limited by both spectral and spatial resolution and as the column density is quite low, we worked with the values derived by *ellfit* as the best-fitting parameters. Therefore, the results are just an estimate. Figure 12 shows the velocity field (left panel), the model (middle panel) and the residual map (right panel). The velocity field reveals a regular rotation pattern with a rotation velocity of 4.4 km s⁻¹. The inclination is the same as the one of NGC 4861, but the cloud rotates under a position angle of 244 $^{\circ}$ (see Table 1). The systemic velocity was measured to be 791 km s⁻¹, which is about 60 km s⁻¹ lower than expected from the rotation of the main body.

5. Discussion

Our analysis has shown that NGC 4861 harbours several outflows, both in H α and HI. In this section, we want to discuss our detections and to make some predictions about the fate of the gas.

5.1. The outflows

Three prominent outflows were detected which show the same kinematic behaviour in H α and HI. In all cases, the neutral outflowing gas is much more extended than the ionised gas. This is probably due to the much lower column densities of the ionised gas, which means that the sensitivity of the FP data is not high enough to detect it everywhere. We showed in Sect. 3.3 that the HI column density (see Fig. 3, upper left panel) is differently distributed at the positions of the outflows in comparison to the rest of the galaxy. In the areas of expanding gas the distance between two neighbouring intensity contours becomes much larger. This means that the gas density is higher in these areas, which fits to the image of gas which is blown out and is at the same time moving more gas out of the GEHR and therefore enhancing the density.

From the geometry and the similar expansion velocities the blue- and red-shifted outflows to the south and to the north of the GEHR probably belong to the expanding supergiant shell SGS4 detected by van Eymeren et al. (2007). They found SGS4 in five highly-resolved spectra with increasing line of sight velocities of about 110 km s⁻¹ blue-shifted and 60 km s⁻¹ red-shifted towards the centre of the GEHR. In H α , we could only measure line of sight velocities at the edges of the GEHR (about 30 km s⁻¹) because areas of very high intensity (i.e., the GEHR) are contaminated by a high artificial velocity gradient due to blurring inside the detector or a saturation problem of the photon counting system (see van Eymeren 2008). The HI velocity field also shows

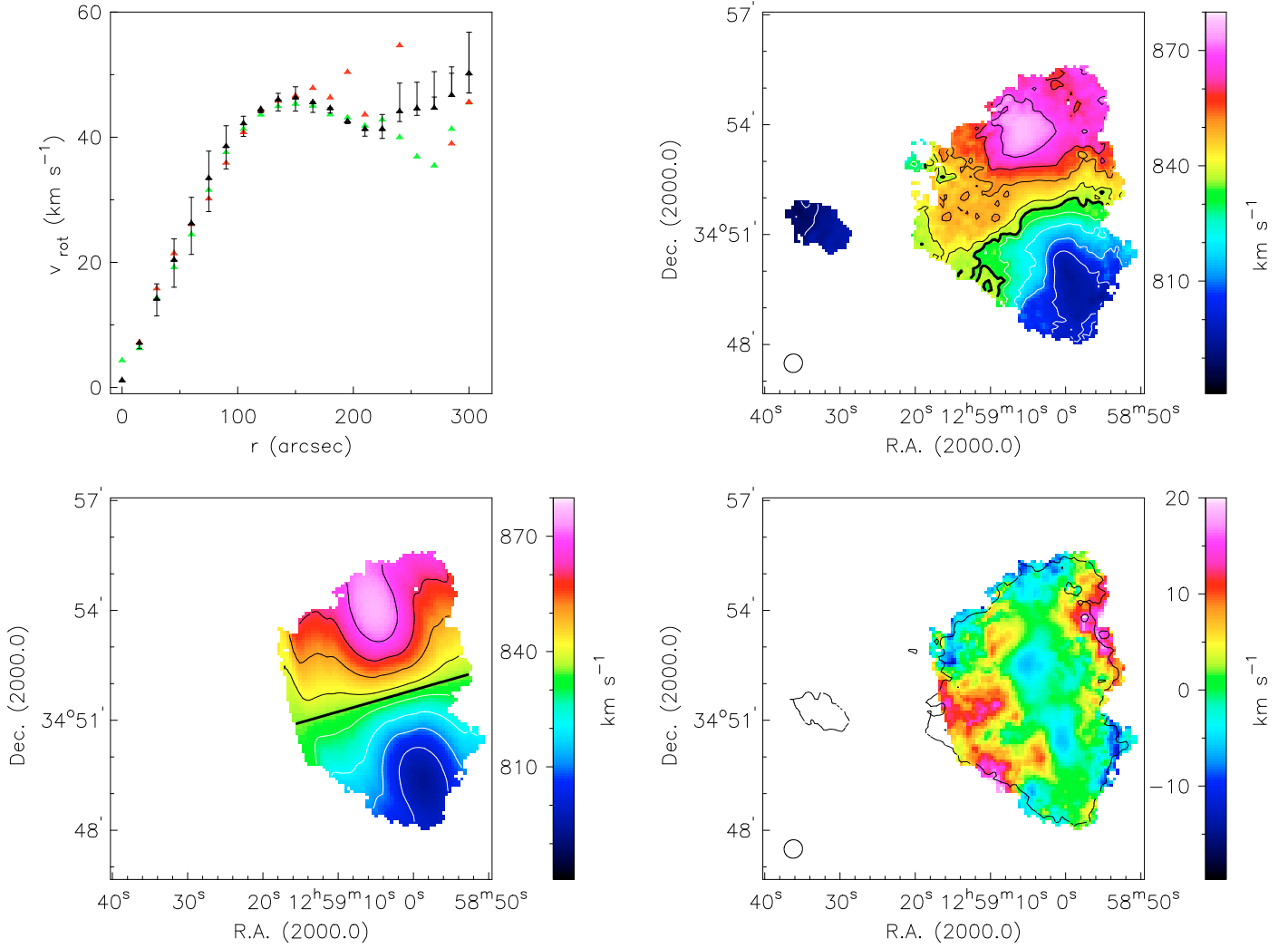


Fig. 8. The HI rotation curve of NGC 4861. *Top left:* different approaches for deriving the rotation curve. The black symbols represent the best-fitting parameters derived in an iterative approach. The error bars indicate receding and approaching side. The green (light grey) curve was derived by taking the initial estimates and keep them fixed, the red (dark grey) curve by taking the best-fitting parameters and let them vary. *Top right:* the HI velocity field. *Bottom left:* the model velocity field, created by the best-fitting parameters. *Bottom right:* the residual map after subtracting the model from the original velocity map.

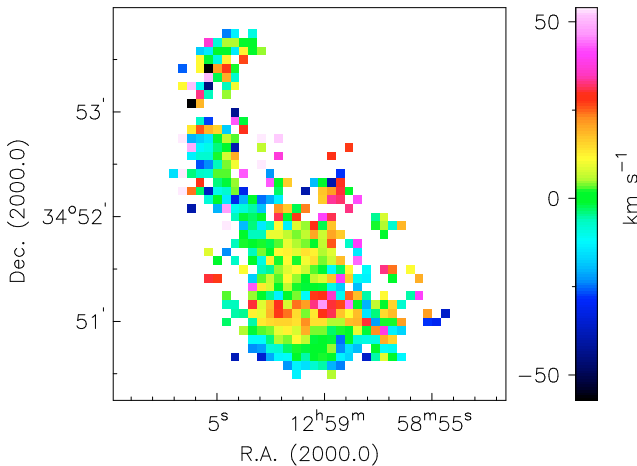


Fig. 9. A comparison of the neutral and ionised gas velocities. The residuals after subtracting the HI velocity field from the H α velocity field are shown.

expanding gas in the central parts of the GEHR, but only with velocities of about 25 km s^{-1} blue- and redshifted. This could

be a resolution effect as the GEHR is only represented by a few beams in HI. Furthermore, the HI has at least partly been ionised, which is indicated by the lower column density (see Sect. 3.3). Taking all this together, we come to the conclusion that the fast expanding supergiant shell exists, at least in H α .

Outflowing gas was also detected west of NGC 4861 at the positions of the supergiant shells. Looking at the H α image it seems that all three shells (SGS1, SGS2, SGS3) are connected and form indeed one single huge shell. However, the kinematic analysis showed that only SGS1 and SGS2 are expanding, whereas SGS3 shows no significant velocity offset along the line of sight (see Sect. 4.1). Several scenarios are plausible: all three shells could have the same origin, but the HI column densities close to SGS3 were higher and forced the gas to slow down more rapidly. However, looking at Fig. 4, one can see that SGS3 is located in an area of lower HI column density than the other two supergiant shells. It is also possible that SGS3 originates from a different star formation event, which could be examined by a chemical analysis of the gas. A third option is that the shell expands perpendicularly to the line of sight.

In the area of SGS5, a faint blue-shifted component with a high velocity offset of about 80 km s^{-1} was detected in H α (see

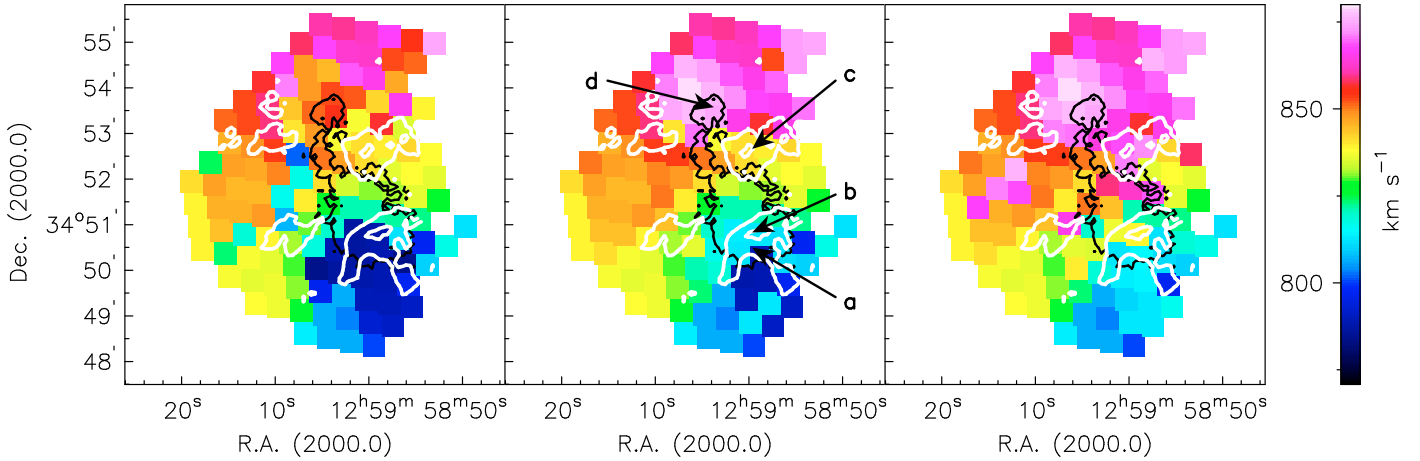


Fig. 10. Gaussian decomposition of the HI emission line. Blue-shifted (*left panel*), main (*middle panel*) and red-shifted (*right panel*) components of the HI velocities are shown. Note that regions where no blue- or red-shifted component was detected were filled with the main component. Overlaid in white are the HI velocity dispersion contours at 18 and 22 km s⁻¹ as well as the outermost H α intensity contour in black. The areas from where we extracted example spectra are labelled.

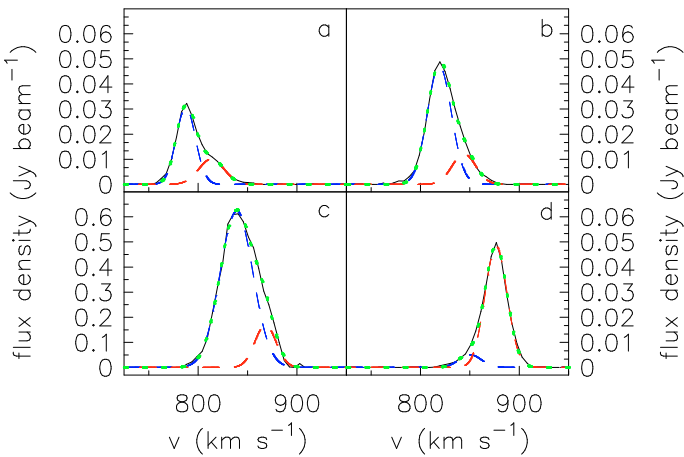


Fig. 11. Some example HI line profiles (black solid lines): **a**) the blue-shifted outflow south of the GEHR; **b**) the red-shifted counterpart north of the GEHR; **c**) the red-shifted outflow close to the supergiant shells; **d**) the potential blue-shifted component at SGS5. The Gaussian profiles fitted to the single components are overlaid in blue (dark grey) and red (light grey), the resulting sum of the profiles is plotted with a green (light grey) short-dashed line.

Sect. 4.1). This area was not covered by the echelle spectra analysed in van Eymeren et al. (2007), and as the H α emission is very weak, we do not want to confirm its existence at this stage. In case it is real emission, NGC 4861 becomes an interesting object because it then harbours two supergiant shells with very high expansion velocities, which requires a very high energy input and which enhances the chance of a galactic wind. The HI spectra in the area of SGS5 reveal a blue-shifted component with an expansion velocity of 20 km s⁻¹, which is far below the offsets measured in H α . But again, this could be a resolution effect.

Where does the gas get its energy from? The outflows close to the GEHR are most probably driven by the star formation activity within this H II region. Barth et al. (1994) estimated the age of the star cluster in the centre of the GEHR to be 4.5 Myr, which was confirmed later by Fernandes et al. (2004). Assuming a constant expansion velocity of 30 km s⁻¹ and a deprojected distance of 545 pc, we get an estimate for the expansion age of the blue- and red-shifted outflow south of the GEHR of 1.8×10^7 yr. For the red-shifted outflow north of the GEHR the expansion age is even higher with 3.6×10^7 yr (assumed deprojected

distance of 1090 pc, expansion velocity of 30 km s⁻¹). This means that either the gas was ionised by a former star formation event or the expansion velocity has decreased over time. This result is in good agreement with similar estimates done for other galaxies (van Eymeren et al. 2009). However, studies by Sramek & Weedman (1986) found a deficiency of nonthermal emission in NGC 4861, which indicates a lack of supernova remnants and therefore a lack of past star formation events. This would then mean that the gas was indeed ionised by the current star formation event and is already losing kinetic energy. On the other hand, we probably only miss the high velocity gas due to the technical problems described above. If we take the expansion velocities of, e.g., 110 km s⁻¹ measured by van Eymeren et al. (2007), we get an expansion age of 4.8×10^6 yr at a travel distance of 545 pc, which is very close to the age of the star cluster.

We have also looked at the distribution of the hot ionised gas. XMM-Newton data show that NGC 4861 has a very luminous X-ray source in the centre of the GEHR (Stobbart et al. 2006), which would explain the high expansion velocities detected in the echelle spectra. In the area of SGS5, however, no X-ray emission can be seen.

5.2. Outflow or galactic wind?

We now want to compare the expansion velocities of the detected outflows with the escape velocities of NGC 4861 in order to make some statements about the fate of the gas. As shown in van Eymeren (2008), the pseudo-isothermal (ISO) halo represents the observed density profiles of dwarf galaxies much better than the NFW halo, at least in the inner kpc. As the outflows are generally close to the dynamic centre, we decided to estimate the escape velocities from the ISO halo. We followed the same procedure as described in van Eymeren et al. (2009). The circular velocity was measured from the rotation curve to be 46 km s⁻¹ (see Table 1). In Fig. 13 we plotted the escape velocity for two different halo radii $r_{\max} = 11$ kpc (dotted line) and $r_{\max} = 22$ kpc (solid line). The lower value of r_{\max} was chosen to equal the size of the HI distribution so that the corresponding curve is a lower limit for the escape velocities. The observed rotation curve including receding and approaching side is indicated by small grey triangles. The expanding gas structures are marked by large black triangles. We corrected the values for an inclination of 65°

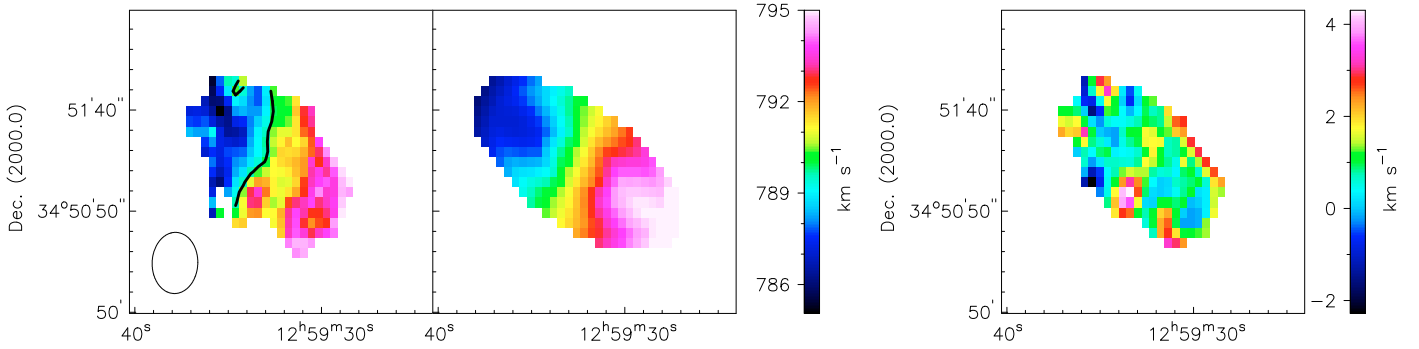


Fig. 12. A kinematic study of the HI cloud NGC 4861 B. Velocity field (*left panel*) with a black contour at $v_{\text{sys}} = 791 \text{ km s}^{-1}$, model velocity field (*middle panel*) and residual map (*right panel*).

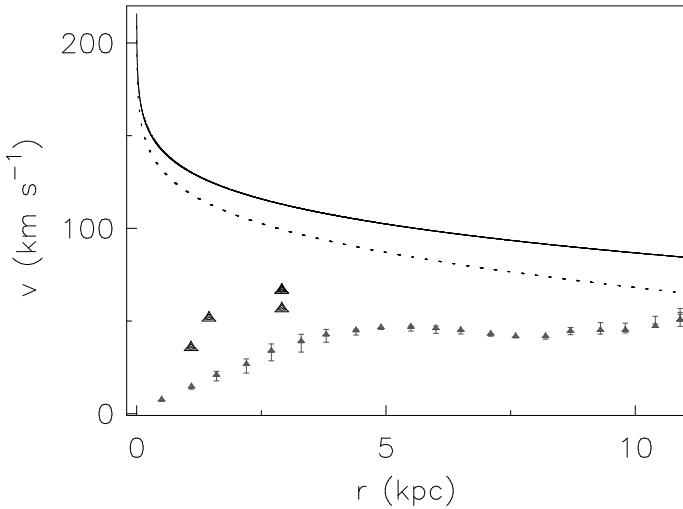


Fig. 13. Escape velocity for a pseudo-isothermal halo of $r_{\text{max}} = 11 \text{ kpc}$ (dotted line) and $r_{\text{max}} = 22 \text{ kpc}$ (solid line). The observed rotation curve is indicated by small grey triangles. The error bars represent receding and approaching side. The expanding gas structures are marked by large black triangles.

as calculated in Sect. 4.2, which leads to an increase in velocity of about 10%.

As Fig. 13 shows, the expansion velocities of all outflows stay far below the escape velocities, which makes it impossible for the gas to leave the gravitational potential of the galaxy. However, as discussed in Sect. 5.1, we probably missed the high velocity parts of the supergiant shell SGS4 expanding from the GEHR because of the artificial emission. We did also not include the fast expanding supergiant shell SGS5. SGS4 is close to the dynamic centre where the escape velocities are high. SGS5, whose existence first needs to be confirmed by, e.g., obtaining a slit spectrum, is about 4 kpc away from the dynamic centre and expands with 80 km s^{-1} , which means that here, the chance of a galactic wind is strongly increased.

5.3. A comparison with NGC 2366

We want to compare our results with the results from a previous study of the irregular dwarf galaxy NGC 2366 (van Eymeren et al. 2009). NGC 2366 is very well suited to be compared to NGC 4861 because not only their optical appearances are very similar, but also the parameters describing the kinematic properties of the neutral gas are similar for both galaxies.

Optical images of NGC 2366 and NGC 4861 show that their H α luminosities are dominated by a GEHR in the south. At the edge of the star distribution at the northernmost tip, both galaxies show shell-like structures. In case of NGC 2366 we detected an associated star cluster, but in NGC 4861 it is not that obvious.

The morphological properties of the neutral gas are different. NGC 2366 shows a distribution that is more patchy and a velocity field that is more perturbed. The main drivers for the distortions are probably the GEHR and the weak spiral arms. NGC 4861 shows no evidence for spiral arms. Nevertheless, this galaxy seems to be more active than NGC 2366 as it harbours at least one fast expanding bubble (see Sect. 5.1).

Most of the detected outflows are in the vicinity of the GEHRs, which is to be expected because the GEHRs are the centres of star formation activity. NGC 4861 also shows outflowing gas clearly outside the disc, but with quite moderate expansion velocities. All outflows were detected in both H α and HI. The 50 km s^{-1} outflow in NGC 2366, however, was only detected in H α , which is probably an effect of age and energy input. In most cases, a former star formation event or decreasing expansion velocities are needed to explain the current position and expansion velocity of the gas structures.

The main result of our study is that we did not detect any galactic wind in any of the two galaxies. As already discussed in van Eymeren et al. (2009), this is in good agreement with simulations by Mac Low & Ferrara (1999) and Silich & Tenorio-Tagle (1998). However, in both galaxies the escape velocity drops significantly at greater distances from the dynamic centre. In NGC 4861 we even detected gas far outside the galactic disc, but it expands with quite moderate velocities. The gas with high velocity offsets is located in the disc.

5.4. NGC 4861 B

We obtained a deep V band image which confirms the result from Wilcots et al. (1996) who did not detect an optical counterpart on a DSS image. Furthermore, we could show that the HI cloud seems to be kinematically decoupled from the main body as its systemic velocity is about 60 km s^{-1} lower and as it is rotating in the opposite direction of NGC 4861. Nevertheless, the distortions in the eastern part of NGC 4861 suggest that both systems interact with each other.

We got an idea of the kinematic properties of NGC 4861 B by fitting ellipses to the HI distribution (see Sect. 4.5). This means that the parameters given in Table 1 are just estimates. Whereas the systemic velocity and the position angle are well-defined, the uncertainties of the inclination and therefore the

inclination corrected rotation velocity and the dynamic mass are high. Nevertheless, the velocity field (see Fig. 12) shows a regular rotation pattern and the residual map is smooth. A better measurement of the inclination and a higher spatial resolution and sensitivity of the HI data are needed in order to investigate the origin of this HI cloud.

6. Summary

Fabry-Perot interferometric data and HI synthesis observations were used to get new insights into the morphology and the kinematics of the neutral and ionised gas components in the nearby irregular dwarf galaxy NGC 4861. Additionally, we examined the HI cloud NGC 4861 B in more detail. The most important results are now briefly summarised.

Both gas components show a very similar behaviour. We detected three prominent outflows, a blue- and a red-shifted outflow in the south of the GEHR with expansion velocities of about 25 km s^{-1} (HI) and 30 km s^{-1} (H α) together with a blue- and red-shifted outflow in the north of the GEHR with an expansion velocity of about 25 km s^{-1} (HI, only red-shifted component detected) and 30 km s^{-1} (H α). These outflows are most probably part of the fast expanding supergiant shell SGS4 detected in van Eymeren et al. (2007). Furthermore, a red-shifted outflow was detected close to the supergiant shells in the west of the tail with an expansion velocity of about 30 km s^{-1} (HI and H α). All outflows are more extended in HI than in H α . A comparison of the expansion velocities with the escape velocity of the galaxy using the pseudo-isothermal halo model revealed that the gas stays gravitationally bound. This is in good agreement with a previous study of the dwarf galaxy NGC 2366 (van Eymeren et al. 2009).

A deep V-band image suggests that the HI cloud NGC 4861 B has no optical counterpart as we did not detect any star association down to a 3σ detection limit of $27.84 \text{ mag arcsec}^{-2}$ in V. Nevertheless, it shows a regular rotation. From our results, it is not possible to define its origin.

Acknowledgements. The authors would like to thank Eric Wilcots for providing the VLA HI data and the R-band image of NGC 4861, for stimulating discussions and the invitation to Madison. We also thank the referee, Kambiz Fathi, whose persistent feedback helped us to deepen our knowledge about handling and interpreting line profiles.

This work was partly supported by the Deutsche Forschungsgesellschaft (DFG) under the SFB 591, by the Research School of the Ruhr-Universität Bochum, by the Australia Telescope National Facility, CSIRO, and by the DAAD. It is partly based on observations collected at the Observatoire de Haute-Provence and at the Centro Astronómico Hispano Alemán (CAHA) at Calar Alto, operated jointly by the Max-Planck Institut für Astronomie and the Instituto de Astrofísica de Andalucía (CSIC). It is also partly based on archival VLA data of the National Radio Astronomy Observatory. The NRAO is a facility of the National Science Foundation operated under cooperative agreement by Associated Universities, Inc. We made extensive use of NASA's Astrophysics Data System (ADS) Bibliographic Services and the NASA/IPAC Extragalactic Database (NED) which is operated by the Jet Propulsion Laboratory, California Institute of Technology, under contract with the National Aeronautics and Space Administration.

Appendix A: H α image and extension of the catalogue of ionised gas structures

Here, the continuum-subtracted H α image is again presented with a contrast different from the one in Fig. 1 in order to

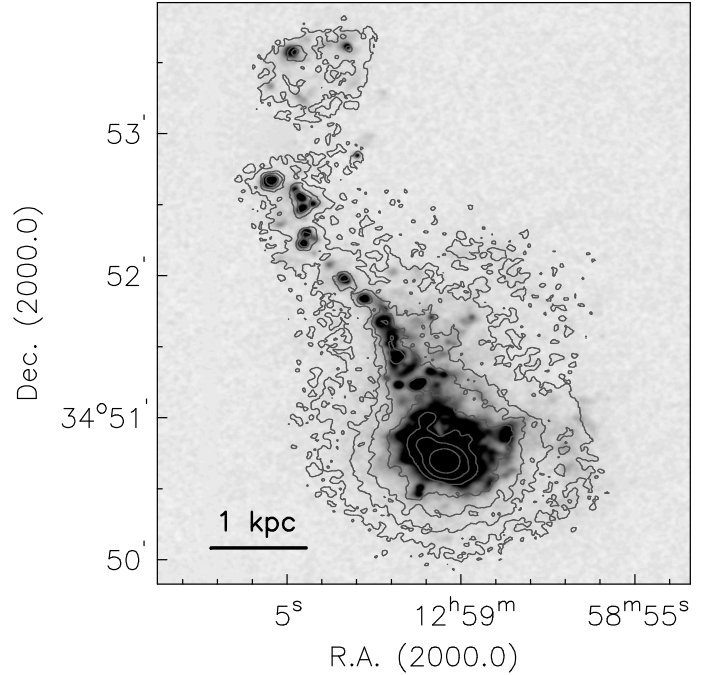


Fig. A.1. Continuum-subtracted H α image of NGC 4861. The contrast is chosen in a way to demonstrate the small-scale structures. Overlaid in grey are the FP H α intensity contours at $0.5 (3\sigma)$, 5, 10, 20, 50, 100, and 300 (arbitrary units).

emphasise the small-scale structures (see Fig. A.1). For a comparison, the FP H α intensity contours are overlaid in grey.

References

- Barth, C. S., Cepa, J., Vilchez, J. M., & Dottori, H. A. 1994, *AJ*, 108, 2069
 Begeman, K. G. 1989, *A&A*, 223, 47
 Bomans, D. J. 2005, in *The Evolution of Starbursts*, AIP Conf. Proc., 783, 98
 de Vaucouleurs, G., de Vaucouleurs, A., Corwin, H. G., et al. 1991, *Third Reference Catalogue of Bright Galaxies* (Berlin, Heidelberg, New York: Springer-Verlag), Vol. 1–3, XII, 2069, 7
 Fernandes, I. F., de Carvalho, R., Contini, T., & Gal, R. R. 2004, *MNRAS*, 355, 728
 Gach, J.-L., Hernandez, O., Boulesteix, J., et al. 2002, *PASP*, 114, 1043
 Gil de Paz, A., Madore, B. F., & Pevunova, O. 2003, *ApJS*, 147, 29
 Hodge, P., Strobel, N. V., & Kennicutt, R. C. 1994, *PASP*, 106, 309
 Hunter, D. A., Hawley, W. N., & Gallagher, J. S. 1993, *AJ*, 106, 1797
 Mac Low, M., & Ferrara, A. 1999, *ApJ*, 513, 142
 Martin, C. L. 1998, *ApJ*, 506, 222
 Moiseev, A. V., & Egorov, O. V. 2008, *Astrophys. Bull.*, 63, 181
 Richter, G. M., Lorenz, H., Bohm, P., & Priebe, A. 1991, *Astron. Nachr.*, 312, 345
 Silich, S. A., & Tenorio-Tagle, G. 1998, *MNRAS*, 299, 249
 Sramek, R. A., & Weedman, D. W. 1986, *ApJ*, 302, 640
 Stobart, A.-M., Roberts, T. P., & Wilms, J. 2006, *MNRAS*, 368, 397
 Thuan, T. X., Hibbard, J. E., & Lévrier, F. 2004, *AJ*, 128, 617
 van der Hulst, J. M., Terlouw, J. P., Begeman, K. G., Zwitter, W., & Roelfsema, P. R. 1992, in *Astronomical Data Analysis Software and Systems I*, ed. D. M. Worrall, C. Biemesderfer, & J. Barnes, ASP Conf. Ser., 25, 131
 van Dokkum, P. G. 2001, *PASP*, 113, 1420
 van Eymeren, J. 2008, Ph.D. Thesis, Astronomisches Institut der Ruhr-Universität Bochum, Germany
 van Eymeren, J., Bomans, D. J., Weis, K., & Dettmar, R.-J. 2007, *A&A*, 474, 67
 van Eymeren, J., Marcelin, M., Koribalski, B., et al. 2009, *A&A*, 493, 511
 Wilcots, E. M., Lehman, C., & Miller, B. 1996, *AJ*, 111, 1575